

*REPORT OF
RESEARCH CENTER OF ION BEAM TECHNOLOGY
HOSEI UNIVERSITY
Supplement No.40. March 2022*

*Proceedings of The 40th Symposium on Materials Science and Engineering,
Research Center of Ion Beam Technology, Hosei University*

Research Center of Ion Beam Technology, Hosei University
Koganei, Tokyo 184-8584, Japan

REPORT OF
RESEARCH CENTER OF ION BEAM TECHNOLOGY
HOSEI UNIVERSITY
Supplement No.40. March 2022

*Proceedings of The 40th Symposium on Materials Science and Engineering,
Research Center of Ion Beam Technology, Hosei University*

PREFACE

This proceeding contains the papers presented at the 40th symposium on “Materials Science and Engineering” held online, December 8, 2021. This symposium is annually held by the Research Center of Ion Beam Technology, Hosei University.

The 40th symposium focused on topics of Research and Development of Advanced Materials. We hope this proceeding will be useful to all those interested in those growing and evolving technologies.

We thank all participants for their beautiful cooperation which made this symposium a successful enterprise. We also thank the board of trustees of Hosei University for their financial support.

Tomoaki Nishimura
Editor

December, 2021

CONTENTS

Contributed Papers

1. CURRENT-VOLTAGE PROPERTIES OF SCHOTTKY CONTACT FORMED BY COPPER LAYER DEPOSITED ON ION-IMPLANTED P-TYPE DIAMONDS <i>M. YOSHIHARA, Y. SEKI, Y. HOSHINO, and J. NAKATA</i>	1
2. ANALYSIS OF Cs REMOVAL PROCESS FROM PHYTOLITHS BY FIB-TOF-SIMS <i>A. KAWASUGI, N. GOMYO, M. MORITA, and T. SAKAMOTO</i>	6
3. SMOOTH SECTIONING OF BIOLOGICAL SAMPLES BY FIB-TOF-SIMS <i>T. GOTO, H. TAKEUCHI, M. SHU, R. SAITO, K. MATSUSHIMA, M. SAITO, S. HANADA, N. KOJIMA, M. MORITA, and T. SAKAMOTO</i>	10
4. INDIVIDUAL SHAPE AND COMPOSITION ANALYSIS OF URBAN ATMOSPHERIC AEROSOLS USING FIB-TOF-SIMS <i>N. KATOH, K. SAKAI, M. MORITA, and T. SAKAMOTO</i>	16
5. INFLUENCE OF RESIDUAL Ga₂O₃ AND Cs ON THE INCREASE IN THE MAXIMUM QUANTUM EFFICIENCY OF NEA-GaAs BY A TWO-STEP THERMAL CLEANING PROCESS <i>Y. SADA, M. JONO, D. KOBAYASHI, Y. YOSHITAKE and T. MEGURO</i>	21
6. ESTIMATION OF EXCITATION DENSITY OF REPORTED TWO-PHOTON PHOTOLUMINESCENCE INTENSITY DISTRIBUTIONS AT A DISLOCATION IN AN n-GaN LAYER ON A M-3D SUBSTRATE <i>K. MOCHIZUKI, H. OHTA, F. HORIKIRI, and T. MISHIMA</i>	27
AUTHOR INDEX	30

CONTRIBUTED PAPERS

CURRENT-VOLTAGE PROPERTIES OF SCHOTTKY CONTACT FORMED BY COPPER LAYER DEPOSITED ON ION-IMPLANTED P-TYPE DIAMONDS

Minami Yoshihara^{#1}, Yuhei Seki, Yasushi Hoshino^{#2}, Jyoji Nakata
Kanagawa University, 2946, Tsuchiya, Hiratsuka, Kanagawa 259-1293, Japan

Abstract

We have formed a Schottky contact on p-type diamond substrates doped only by boron ion implantation process. The doping concentration in the drift layer was $4 \times 10^{18} \text{ cm}^{-3}$ and that beneath the Ohmic contact layer was about $1 \times 10^{21} \text{ cm}^{-3}$ in order to reduce the contact resistance at the Ohmic contact. We investigate the rectifying properties for the Schottky electrode fabricated by copper layer. The observed current between two Ohmic electrodes linearly depended on the applied voltage. From the I - V characteristics between the Ohmic and Schottky contacts, the rectification behavior was not clearly observed for the case of copper electrode, and rectification ratio, which is the current ratio of forward direction to reverse direction, was considerably low.

I. Introduction

Diamond is expected for a candidate of future power devices due to excellent material properties such as wide band gap, high carrier mobility, and high break-down electrical field¹⁻⁵). One of the main subjects in the device fabrication on diamond is the impurity doping with well controlling p-type and n-type conduction. Here, the impurity doping with ion-beam technology is known as an essential process in semiconductor fabrication to dope impurities in the designated area and depth with an accurate concentration, being widely used in Si technology today. However, the electrical activation of impurities doped in diamond with ion implantation technique has not succeeded for a long period. In 2019, we practically realized the impurity activation of the p-type B-implanted diamond by well controlling the conditions of implantation and activation annealing⁶). Moreover, we fabricated Schottky barrier diode (SBD) consisting of an Al layer on p-type diamond formed by B-implantation and confirmed rectifying properties in I - V measurements⁷). In this study, we investigated SBD properties analyzed by I - V measurements for various kinds of metals.

II. Experiment

We purchased high-quality type IIa diamond substrates synthesized by chemical vapor deposition (CVD) method from Element Six Ltd. B ions at the incident energies from 5 to 60 keV were implanted in the chemically cleaned diamond substrates at room temperature (RT) with a uniform doping concentration of $3.5 \times 10^{18} \text{ cm}^{-3}$ from the surface to 100 nm depth. In addition, we excessively implanted B ions in the area of Ohmic electrodes with a high concentration of 10^{21} cm^{-3} to obtain good Ohmic contact. Fig. 1 shows the simulated B depth profile according to TRIM calculation⁸). After the above B-doping process, the sample surface was covered with a thin SiO₂ film with about 100 nm

^{#1} e-mail: r201803693eq@jindai.jp, ^{#2} yoshino@kanagawa-u.ac.jp

thick by a RF sputtering deposition method to protect the surface roughness generated in high-temperature annealing. The activation annealing was performed at 1300°C for 2 h in Ar ambience. The capped SiO₂ layer was then removed by diluted HF solution with 5 % concentration after the activation annealing. The detailed process can be shown in the previously published papers^{6,7,9,10}.

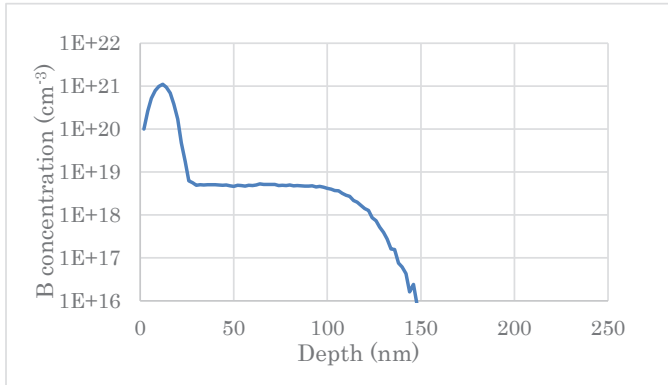


Fig. 1: Simulated B depth profile according to TRIM calculation.

The B-implanted substrate was finally deposited Ohmic and Schottky electrodes by a magnetron sputtering method on the designated area through precisely processed mask patterns. The optical microscope image of the diamond substrate deposited with Ohmic and Schottky electrodes is shown in Fig. 2 and the schematical cross-sectional image depicted along the dashed line in Fig. 2 is shown in Fig. 3. The roundly shaped pattern existent in the center of the sample corresponds to the Schottky electrode consisting of a Cu layer covered with a thick Au layer with the layer thickness of 0.5 μm and 1 μm , respectively. The electrodes surrounding the Schottky electrode are Ohmic ones consisting of Au/Ti bilayer with thickness of 200 and 50 nm, respectively. The Ohmic electrode was deposited through a horseshoe-shaped mask at the substrate temperature of 400°C, and the Schottky electrode was then deposited through a roundly opened mask at RT. We first measured electrical properties at RT based on current-voltage (I - V) measurements between two Ohmic electrodes and Ohmic and Schottky electrodes.

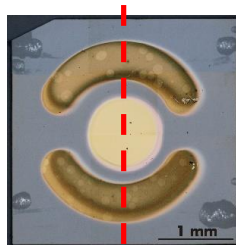


Fig. 2: The optical microscope image of the diamond substrate deposited with Ohmic and Schottky electrodes. Round-shaped electrode in the center of the sample corresponds to the Schottky electrode and two horseshoe-shaped electrodes surrounding the Schottky electrode are Ohmic ones.

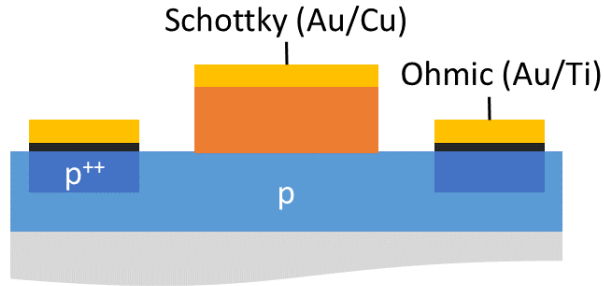


Fig. 3: Schematical cross-section-image depicted along the red dashed line drawn in Fig. 2.

III. Results and discussion

The I - V property measured between two Ohmic electrode comprised with Au/Ti layers is shown in Fig. 4. The I - V property was measured in the applied voltage range of ± 50 V. As shown in Fig. 4, the current was almost linearly increased as a function of the applied voltage, indicating that the Au/Ti electrodes show Ohmic feature. The electrical resistance between them was about 50 k Ω . Fig. 5 shows the I - V property measured between the Au/Ti and Au/Cu electrodes with a linear (a) and a logarithmic (b) scale. It is found in the figures that rectifying property is not clearly observed in the I - V property. The rectifying ratio was only 2.5, which was considerably smaller than that for Al contact reported in the previously published paper ⁷⁾. It is suggested that Cu layer grown on diamond substrate could not be suitable for the Schottky contact.

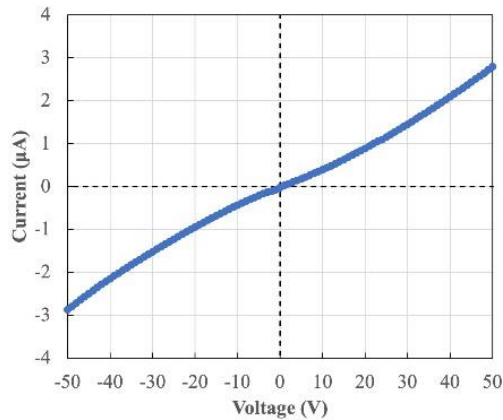


Fig. 4: I - V properties between two Ohmic electrodes consisting of Au/Ti layers.

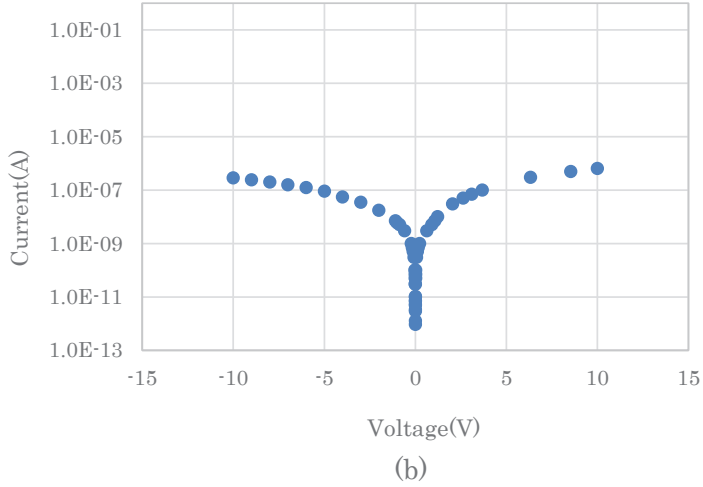
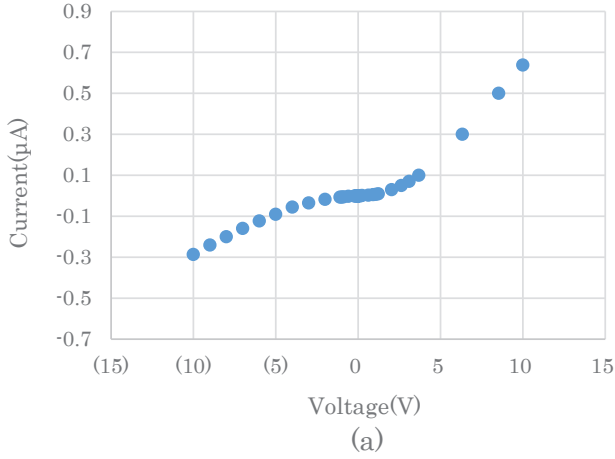


Fig. 5: I - V properties between Au/Ti and Au/Cu electrodes with linear (a) and logarithmic (b) scale.

IV. Conclusions

We investigated a Schottky contact with Cu layer formed on the B-implanted p-type diamond substrate. All B-doping processes were performed by ion implantation technique. The doping concentration in the drift layer was $4 \times 10^{18} \text{ cm}^{-3}$. The Ohmic contacts were formed on heavily B-implanted area with about $1 \times 10^{21} \text{ cm}^{-3}$ concentration. We investigated the rectifying property between Cu and Ti electrodes. As a result, the rectification behavior was not clearly observed, being different from the case of Al and Ti electrodes. It is indicated that Cu contact could not be suitable for the Schottky electrode of p-type diamond.

Acknowledgements

We sincerely appreciate Prof. M. Kasu and Prof. T. Oishi in Saga University for their valuable comments and suggestions on device fabrication. We also thank Mr. Y. Saito for his assistance in the maintenance of experimental apparatuses.

References

- 1) R. S. Balmer, J. R. Brandon, S. L. Clewes, H. K. Dhillon, J. M. Dodson, I. Friel, P. N. Inglis, T. D. Madgwick, M. L. Markham, T. P. Mollart, N. Perkins, G. A. Scarsbrook, D. J. Twitchen, A. J. Whitehead, J. J. Wilman, and S. M. Woollard, *J. Phys. Condens. Matter* **21**, 364221 (2009).
- 2) S. Koizumi, H. Umezawa, J. Pernot, and M. Suzuki, *Power Electronics Device Applications of Diamond Semiconductors* (Woodhead Publishing, Duxford, 2018).
- 3) H. Umezawa, *Mater. Sci. Semicond. Process* **78**, 147 (2018).
- 4) N. Rouger and A. Maréchal, *Energies* **12**, 2387 (2019).
- 5) M. Liao, *Funct. Diam.* **1**, 29 (2021).
- 6) Yuhei Seki, Yasushi Hoshino, and Jyoji Nakata, *Appl. Phys. Lett.* **115**, 072103 (2019).
- 7) Seiya Shigematsu, Toshiyuki Oishi, Yuhei Seki, Yasushi Hoshino, Jyoji Nakata, Makoto Kasu, *Jpn. J. Appl. Phys.* **60**, 050903 (2021).
- 8) J. F. Ziegler, J. P. Biersack, and U. Littmark, *The Stopping and Range of Ions in Solids* (Pergamon Press, Oxford, 1985).
- 9) Yuhei Seki, Yasushi Hoshino, and Jyoji Nakata, *Jpn. J. Appl. Phys.* **59**, 021003 (2020).
- 10) Yuhei Seki, Yasushi Hoshino, and Jyoji Nakata, *J. Appl. Phys.* **129**, 195702 (2021).

Analysis of Cs Removal Process from Phytoliths by FIB-TOF-SIMS

Akihiro Kawasaki¹, Naoki Gomyo², Masato Morita², Tetsuo Sakamoto^{1,2#}

¹*Department of Electrical and Electronic Engineering, Graduate School of Engineering, Kogakuin University, 2665-1 Nakano, Hachioji, Tokyo 192-0015, Japan*

²*Department of Applied physics, School of Advanced Engineering, Kogakuin University, 2665-1 Nakano, Hachioji, Tokyo 192-0015, Japan*

We have been conducting research on the development and analysis of FIB-TOF-SIMS (Focused Ion Beam Time-of-Flight Secondary Ion Mass Spectrometry) instrumentation. As a part of this research, we are also working on the content of research for decontamination activities in the Fukushima Daiichi Nuclear Power Plant accident. In our previous study, we confirmed that Cs is adsorbed on phytolith, which is a silicate material contained in plants. In this study, we analyzed the desorption process of Cs from plant opal using FIB-TOF-SIMS from the viewpoint of heat treatment.

I. Introduction,

The accident at the Fukushima Daiichi Nuclear Power Plant (nuclear accident) in March 2011 released a variety of radioactive materials. Among them, radioactive cesium (¹³⁷Cs) has half-life is about 30 years, so it is concerned long-term environmental problem. Against this background, investigation and research on ¹³⁷Cs have been progressing, and it has been found to be absorbed by plants ^[1] and fine minerals such as mica ^[2].

Plants contain phytoliths (called “plant opals”), which are silicate bodies of several tens of micrometers in size ^[3]. In our laboratory, we have confirmed that phytoliths absorb Cs. Phytoliths account for 3-10 vol.% of plant bodies, and since forests largely cover Fukushima area, they are thought to have a significant influence on the behavior of Cs in the environment. In this study, we analyzed the desorption process of Cs from phytoliths using a focused ion beam time-of-flight secondary ion mass spectrometer (FIB-TOF-SIMS) ^[4] developed in our laboratory. Phytoliths with physisorption of Cs were heat-treated and the behavior of Cs was analyzed.

II. Experimental

The phytoliths were prepared as shown in Figure 1. Under atmospheric conditions, grasses collected in our university campus were ashed at 400°C using an electric stove. The phytoliths were removed by sonication in pure water for 10 minutes. The extracted phytoliths were agitated with Cs solution at 500 rpm for 24 h to physically adsorb Cs. The phytoliths were then heat-treated at 400°C, 600°C, and 900°C for 1 hour, respectively. In addition, a 600°C heat treatment for 6 hours was also prepared. In order to take into account the structural change caused by heating, we also prepared the extracted phytoliths that were heat-treated and then agitated with Cs solution. The temperature conditions for the latter were 600°C and 900°C, respectively.

Since phytoliths are not electrical conductor, they are charged by the ion beam irradiation during TOF-SIMS analysis. The phytoliths obtained by the above process were pressed onto a Pb plate to ensure the conductivity. Then the Pb plate was fixed on an Al pellet in a sample holder.

e-mail: ct13087@ns.kogakuin.ac.jp

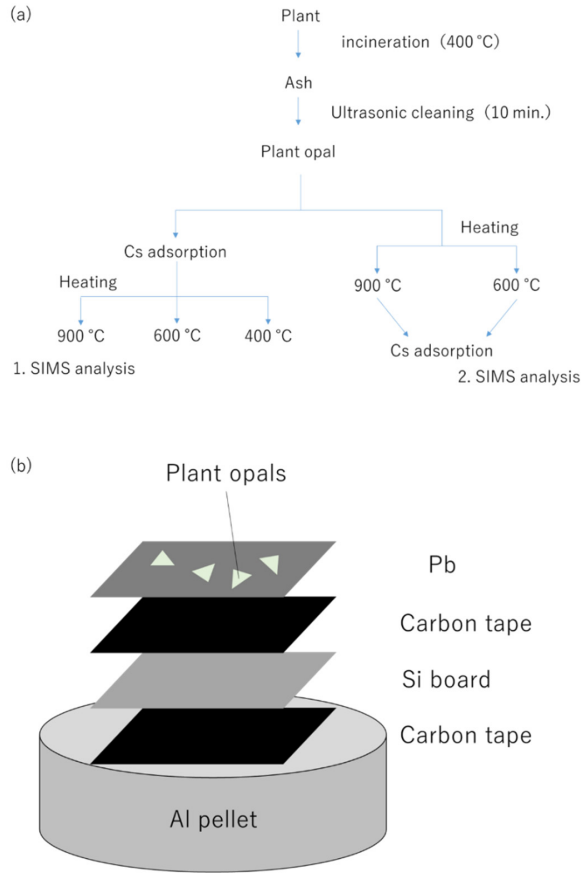


Fig. 1. Sample preparation image
 (a) Flowchart of heating conditions, (b) Sample mounting for TOF-SIMS

III. Result and Discussion

The results of the analysis of heat-treated Cs-containing phytoliths are shown in Fig. 2. When analyzing the phytoliths, the surface and the interior of the phytoliths were compared by sputtering of a part of analyzing area. In cases of 1 hr heating at 400, 600 and 900 °C, Cs was detected from both surface and interior. As for 6 hrs heating at 600°C, less amount of Cs was detected. This suggests that the limiting factor is not the temperature (at least 600°C), but diffusion coefficient within phytoliths. The detailed structure of phytoliths is not clear. But if it has pore structure, Cs reaches at the surface while desorption and adsorption of the inner surface of the pores. Therefore diffusion coefficient may play an important role of the desorption process.

Next, after the additional heat-treated samples were stirred with Cs solution and the TOF-SIMS imaging results are shown in Fig.3. A part of imaging area was presputtered in order to analyze the inside of the phytoliths. In both temperatures, there was no Cs inside the phytoliths. This means that heat treatment at 600 and 900°C alters surface structures of the phytoliths, such as shutting the pores at the surface as shown in Fig.4.

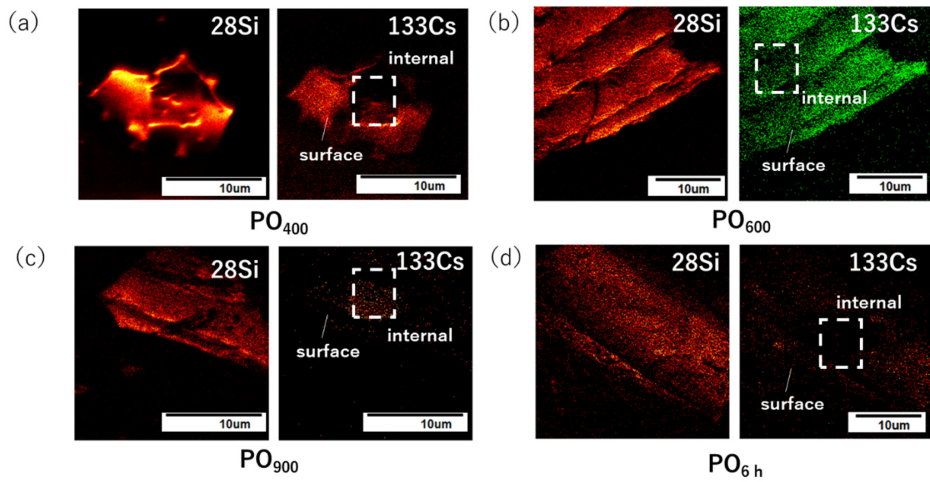


Fig.2. TOF-SIMS images of Phytoliths agitated by Cs after heated at (a)400°C (b)600°C (c)900°C for 1 hr, and (d)600°C for 6h, respectively.

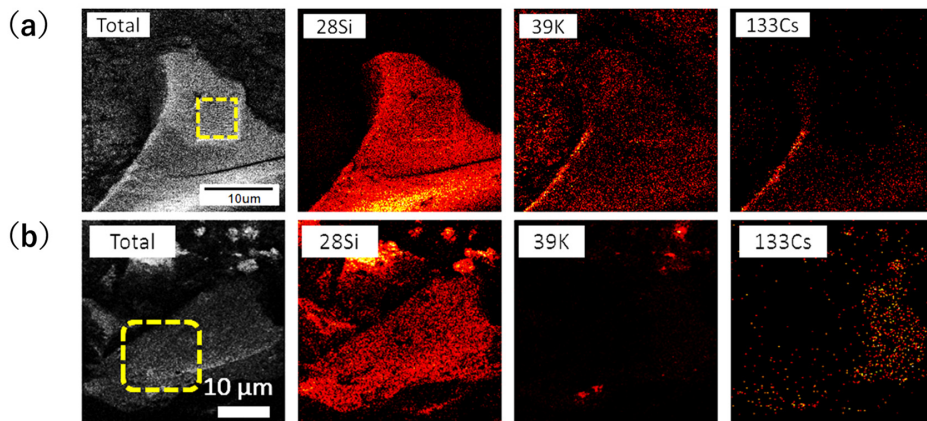


Fig. 3. TOF-SIMS images of the Phytoliths agitated by Cs after heating (a) 600°C (b) 900°C.

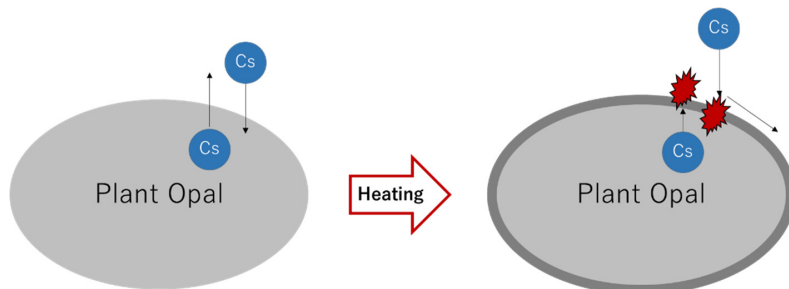


Fig.4. Surface change of phytoliths by high temperature treatment

There is a provision that actual waste treatment be done at 850°C or higher^[5]. As surface modification occurs, Cs is stored in the phytoliths, which is expected to reduce the volume of contaminants.

IV. Conclusion

The Cs desorption process from the phytoliths by heating was confirmed by FIB-TOF-SIMS analysis. In addition, the clarification of the desorption process indicated the validity of the specified temperature for waste treatment.

V. Reference

- [1] Imamura Naohiro et al., *Sci Rep.*, **7**, 1-11 (2017).
- [2] Toshihiro K et al., *Chikyukagaku.*, **49**, 195-201 (2015).
- [3] 菅野一野 他, *Japanese Soc Pedolgy*(in Japanese)., **2**, 78-80 (1958).
- [4] T. Sakamoto *et al. Appl. Surf. Sci.*, **255**, 4, 1617-1680 (2008) .

Smooth sectioning of biological samples by FIB-TOF-SIMS

Tomoki Goto¹, Hyogo Takeuchi², Mizuki Shu¹, Reiko Saito^{2,3},
Kazuya Matsushima⁴, Makoto Saito⁴, Sanshiro Hanada⁴, Nobuhiko Kojima⁴,
Masato Morita¹, and Tetsuo Sakamoto^{1,2#}

¹*Department of Applied Physics, Kogakuin University, 2665-1, Nakano, Hachioji,
Tokyo, 192-0015 Japan*

²*Graduate School of Engineering, Kogakuin University, 2665-1, Nakano, Hachioji,
Tokyo, 192-0015 Japan*

³*Corporate Manufacturing Engineering Center, Toshiba Corporation, 33 Shin Isogo-
cho, Isogo-ku, Yokohama, Kanagawa 235-0017, Japan*

⁴*Department of Life and Environmental System Science, Graduate School of
Nanobioscience, Yokohama City University, 22-2 Seto, Kanazawa-ku, Yokohama,
Kanagawa 236-0027, Japan*

Spheroids, which are three-dimensionally cultured cells that resemble actual living organisms, have been attracting attention. FIB-TOF-SIMS (Focused Ion Beam Time-of-Flight Mass Spectrometry) is capable of simultaneous mass imaging of multiple elements without the need for labeling. FIB-TOF-SIMS is expected to process the spheroid and image the cross-sectional components. However, FIB processing of spheroids larger than 100 μm often results in uneven cross sections due to the so-called curtain effect. The unevenness of the cross-section affects the sputtering and hinders component imaging. In this experiment, we considered the processing of spheroids by FIB from multiple directions to suppress the curtain effect. The curtain effect was evaluated by comparing the processing from one direction and from multiple directions.

I. Introduction

Recently, "spheroids", which are three-dimensionally cultured cells similar to actual living organisms, have been attracting attention [1]. In addition, spheroids containing beads with internal channel-like structures for supplying oxygen and nutrients to the inside of the spheroid have been developed [2]. By creating spheroids with the same number of alginate hydrogel beads as cells, a network-like arrangement of hydrogel beads is created from the surface of the spheroid to the interior. Since the hydrogel beads are mostly water, oxygen, nutrients, and waste products can diffuse and move through the channel-like space formed by the hydrogel beads. In addition, alginate lyase can digest alginate hydrogel beads in a few minutes, creating an actual space. Spheroids have been applied to drug dosing experiments, and the distribution of drugs has mostly been observed by fluorescent labeling and confocal microscopy [3]. However, some drugs cannot be fluorescently labeled, and excessive labeling may alter the kinetics of the drug. Therefore, it is necessary to devise a new method to visualize drug distribution without using fluorescent labeling.

#e-mail:ct13087@ns.kogakuin.ac.jp

The FIB-TOF-SIMS (focused ion beam time-of-flight mass spectrometry) system developed by our laboratory has the highest resolution of 40 nm, which enables simultaneous mass imaging of multiple elements without the need for labeling [4]. In FIB-TOF-SIMS, the spheroid can be processed by FIB and the cross section can be component imaged. However, FIB-TOF-SIMS requires analysis in a high vacuum, and biological samples such as spheroids are susceptible to moisture volatilization, which may alter their composition and structure [5]. FIB-TOF-SIMS is expected to provide a solution to this problem, since both processing and analysis can be performed in the instrument.

However, spheroids has diameters around 100 ~ 400 μm , in such cases so-called “curtain effect” occur. This is because that the FIB is not a parallel beam, but a focused beam. If the processing object is larger, the distance from the beam focal point to the edge of the object has a dispersion. So, the cross-section is not flat, but “wave interdigital” morphology. In this paper, we examined the solution for suppress the curtain effect by cross-sectioning from multiple angle of incidence of the FIB.

II. Experimental

A spheroid used here was made by mixing two-thousands of HuH-7 cells and that of hydrogel beads. The spheroid as fixed on a Si wafer using Ag-paste, and then transferred into the TOF-SIMS stage at room temperature. The FIB was installed at 45° with respect to the surface (substrate) normal. Therefore, in the first processing, the specimen stage was tilted to 45° so as to the FIB axis and substrate surface are parallel. As a result, the top part of the spheroid was sectioned. After that, the tilt was returned to 0° , and the processed cross section was observed by FIB-induced secondary electrons.

Next, the tilt was applied again at 45° and the rotation was set at 45° for machining from the second direction. After the second machining, the tilt was returned to 0° and the machined cross section was observed. This process was also carried out with rotation of 30° and -30° at tilt angle of 45° . The machining conditions are summarized in Table 1. The FIB used in this experiment was Ga^+ , and the acceleration voltage was 30 kV.

Table 1: Processing conditions

	Beam current	Processing time	Processing width	Tilt	Rotation
First direction	1 st 4.2 nA	130 min	13 μm (thickness)	45°	0°
	2 nd 8.4 nA	120 min	100 μm (width)		
Second direction	1.86 nA	42 min	3 μm (thickness) 115 μm (width)	45°	45°
Third direction	1.86 nA	39 min	3 μm (thickness) 104 μm (width)	45°	30°
Fourth direction	1.86 nA	24 min	2 μm (thickness) 111 μm (width)	45°	-30°

III. Results and Discussion

In case of FIB processing of a large sample greater than several hundreds micrometers, so-called curtain effect becomes prominent [6]. Typical result is shown in Fig.1. The

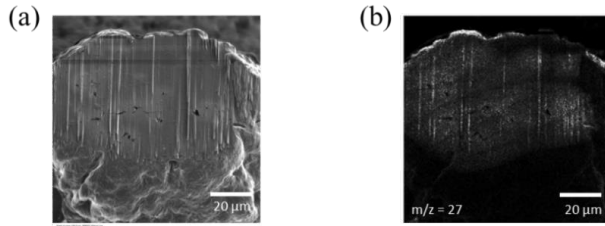


Figure 1: Curtain effect generation.

sample was a spheroid greater than 100 μm , and the cross-sectioning width was identical. As shown in Fig1(a), wave interdigital feature was seen in FIB-induced secondary electron image. Understandably, TOF-SIMS image (C_2H_3^+ , in this case) also exhibit the same effect. It is clear that the smoothing of cross section is essential for highly-reliable imaging.

We considered whether it would be possible to perform a thin finishing process on the cross section cut out from multiple directions after an FIB processing from a direction. The angle of incidence of the FIB in our laboratory is 45° to the sample stage. If the angle of incidence is set to 0° and the specimen stage rotated, it is possible to process the same plane from any direction. Therefore, we devised a eucentric rotation system where the specimen stage is tilted at 45° and rotated at the same angle. The eucentric rotation system is shown in Fig. 2. In this study, we used the eucentric rotation system to verify FIB processing from not only one direction, but from various directions, and to evaluate the occurrence of the curtain effect. Since the quick freezing method for water-containing biological sample is still under investigation, we first evaluated the processing at room temperature.

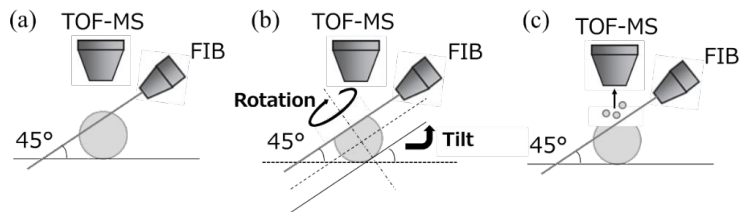


Figure 2: Eucentric rotation system in this study

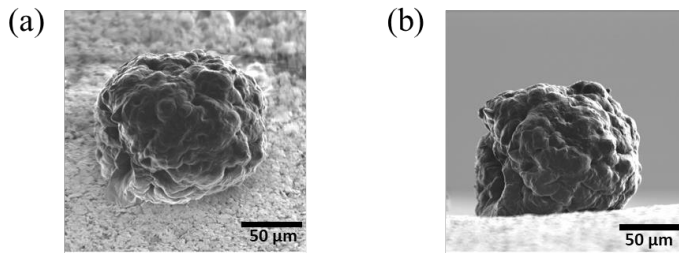


Figure 3: Secondary ion images before processing. (a) tilt at 0° and (b) tilt at 45° .

The eucentric rotation and processing method was applied to a spheroid with a diameter around 150 μm . The secondary ion images of the spheroid before processing at tilt angle of 0° and 45°, respectively in Fig.3(a) and (b). The shape of the spheroid was not a complete sphere but uneven shape. This causes curtain effect. As the first processing,

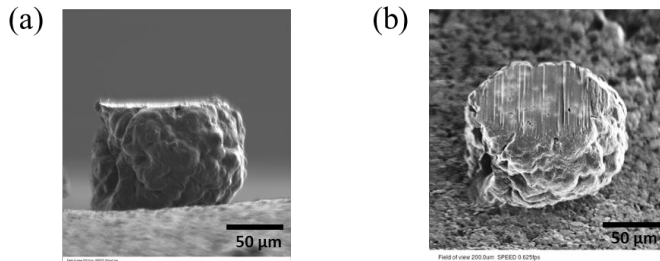


Figure 4: Secondary ion images after processing. (a) a view of the finished machining with the tilt at 45°. (b) a cross-sectional view with the tilt set to 0°.

cross-sectioning of the spheroid with a width of 100 μm . As shown in Fig.4, a cross section was obtained, but a strong curtain effect occur. This was mainly due to the unevenness of the initial shape of the spheroid.

In the next, the processed cross sections from the first direction to the fourth direction are shown in Fig. 5. Here, the cross-sectioning from the fourth direction was observed

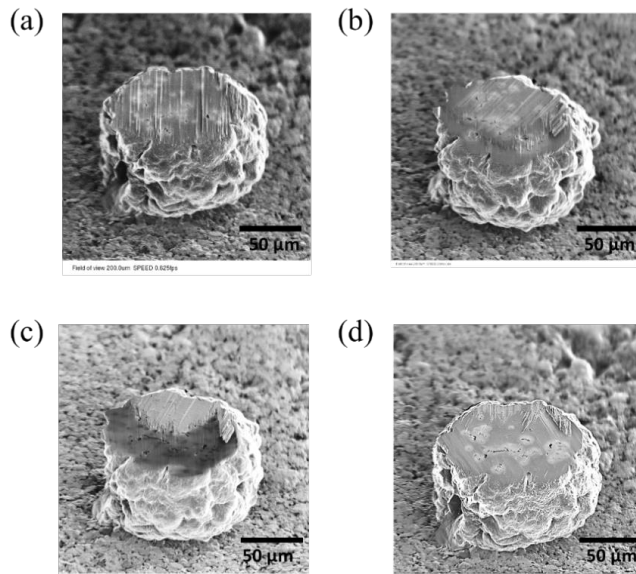


Figure 5: Processed cross section from the first to the fourth direction. (a) shows the machined cross section in the first direction (rotation 0°), (b) in the second direction (rotation 45°), (c) in the third direction (rotation 30°), and (d) in the fourth direction (rotation -30°).

after the rotation was returned to 0° in order to compare it with the cross section of the first direction.

In addition, we compared the processed cross sections of the first direction and fourth direction. First, the secondary ion image of the enlarged cross section is shown in Figure 6. The comparison of the secondary ion images clearly shows that the curtain effect is suppressed.

Next, using ImageJ software, each cross-section was inverse Fourier transformed and the high frequency portions were removed, as shown in Figure 7. This clearly shows the curtain effect. The lines drawn in Fig. 7 were then profiled by luminance. It is shown in Figure 8. Calculating the RMS (root mean square) of the data in Figure 8, we found that $RMS = 9.5$ for the first directional section and $RMS = 4.3$ for the fourth directional section. These values indicate that the variation of luminance has been greatly reduced. This means that the unevenness caused by the curtain effect has been suppressed. This is thought to be due to the smoothing of the convex part of the unevenness by grinding from multiple directions.

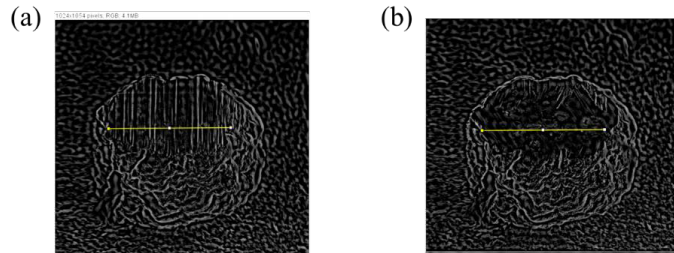


Figure 7: Machined cross-section of the first direction and the fourth direction (high-pass filter). (a) high-pass filtered image for the first directional processed cross section, and (b) high-pass filtered image for the fourth directional processed cross section.

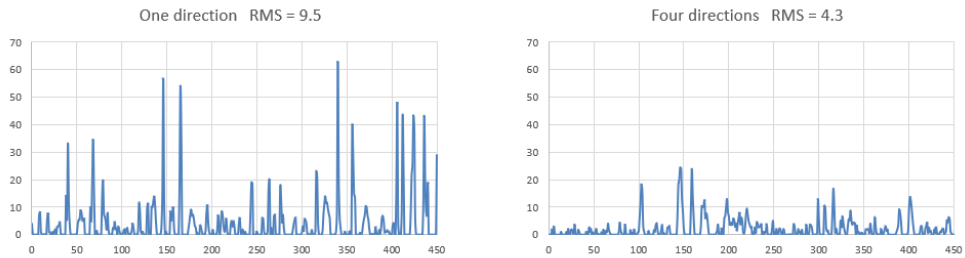


Figure 8: Unevenness profiles for the first direction and the fourth direction. The luminance profile of the horizontal line part of Figure 7.

IV. Conclusions

From the results of this study, we succeeded in machining a smooth cross-section of biological specimens larger than $100 \mu\text{m}$ by scraping the convex part of the unevenness

from multiple directions using the eucentric rotation system. In addition, we were able to quantitatively demonstrate the suppression of unevenness due to the curtain effect by comparing the results with numerical values using RMS. In near future, it will be necessary to perform processing under frozen conditions, which is necessary for biological specimens, and to evaluate the processed cross-section.

V. References

- [1] Y. Miyamoto *et al.*, *Organ Biology*, **27**, 37 (2020).
- [2] N. Kojima *et al.*, *Sensor. Actuat. B-Chem.*, **198**, 249 (2014).
- [3] Delilah F.G. Hendriks *et al.*, *Clinical Pharmacology & Therapeutics.*, **108(4)** 850 (2020).
- [4] T. Sakamoto *et al.*, *Appl Surf Sci*, **255**, 1617 (2008).
- [5] K. Kanenari *et al.*, *e-J Surf Sci Nanotech*, **131**, 14 (2016).
- [6] L.A. Giannuzzi *et al.*, *Micron*, **199**, 30 (1998).

Individual shape and composition analysis of urban atmospheric aerosols using FIB-TOF-SIMS

Noa Katoh¹, Kentaro Sakai², Masato Morita¹, Tetsuo Sakamoto^{1,2#}

¹*Graduate School of Electric Engineering and Electronics, Kogakuin University,
2665-1 Nakano-machi, Hachioji, Tokyo 192-0015, Japan*

²*Department of Applied Physics, Kogakuin University,
2665-1 Nakano-machi, Hachioji, Tokyo 192-0015, Japan*

Minute solid or liquid particles suspended in air are called aerosols. Aerosols can be of natural origin, such as yellow sand, or of anthropogenic origin, such as railroad wear dust. Bulk analysis has been used for the chemical analysis of aerosols with such various sources. However, bulk analysis can only determine the average chemical composition of a group of particles and cannot, in principle, analyze the chemical composition of individual particles ^[1]. In our group, we have developed an FIB-TOF-SIMS (Focused Ion Beam Time-of-Flight Secondary Ion Mass Spectrometer) to analyze the compositional distribution of individual particles ^[2]. Our investigations have revealed that there is a certain correlation between particle composition (source) and particle shape. In addition, it is important to understand the composition and shape of particles originating from urban areas because the traffic volume is relatively high in urban areas and there is concern about the emission of large amounts of aerosols and their health effects on human health ^[3,4]. In this study, we sampled aerosols in Shinjuku area and analyzed them using FIB-TOF-SIMS. In this presentation, we will report the component analysis of urban atmospheric aerosols and the shape characteristics of the particles.

I. Introduction

In the environment where we live, there are many particles of invisible size. These minute solids and liquids suspended in the atmosphere are called aerosols. The sources of aerosols range from natural sources such as pollen and yellow sand to anthropogenic sources such as automobile exhaust and railroad dust. In addition, with the economic development of Asia in recent years, a large number of aerosols have been emitted from industrial areas and have become a factor in air pollution. For chemical analysis of aerosols, bulk analysis has been performed after filter collection. Bulk analysis can obtain quantitative data with high accuracy. However, it can only determine the average chemical composition of a group of collected particles and cannot in principle identify the source of individual particles or analyze their chemical composition ^[1].

In our research group, we have developed an FIB-TOF-SIMS (Focused Ion Beam Time-of-Flight Secondary Ion Mass Spectrometer), which enables to analyze individual particles of aerosols. We have been analyzing the distribution of components from the surface structure to the internal structure of individual particles ^[2]. From previous studies, it has been found that there is some correlation between particle composition (source) and particle shape observed with the FIB-TOF-SIMS. In addition, in urban areas, there is a

#e-mail : ct13087@ns.kogakuin.jp

relatively large amount of traffic such as automobiles and railroads, and there are concerns about the emission of large amounts of aerosols and the health effects of these aerosols on human health [3,4]. Therefore, it is important to understand the composition and shape of urban-derived particles.

In this study, we sampled aerosols in Shinjuku and analyzed them using FIB-TOF-SIMS. As a result of the analysis, it was confirmed that the aerosols suspended in the urban city have a unique structure. In this paper, we report the component analysis of urban atmospheric aerosols by FIB-TOF-SIMS and the shape characteristics of these particles.

II. Experimental

Sampling was done on two days, July 21, 2021, and November 3, 2021. Table 1 shows the details of each sampling date. Figure 1 shows the details of the sampling sites. The sampling sites were located in the Shinjuku campus of Kogakuin University. The sampling point was located facing the road, with Shinjuku station about 450 m away.

Table 1: Sampling details

Sampling dates	Sampling time	Flow rate (L/min)
2021/7/21	1 : 13:25 ~ 13:55	1.5
	2 : 13:55 ~ 14:25	
	3 : 14:25 ~ 14:55	
	4 : 14:55 ~ 15:25	
	5 : 15:25 ~ 15:55	
	6 : 15:55 ~ 16:25	
2021/11/3	1 : 12:15 ~ 14:15	1.5
	2 : 14:25 ~ 15:25	
	3 : 15:35 ~ 17:15	

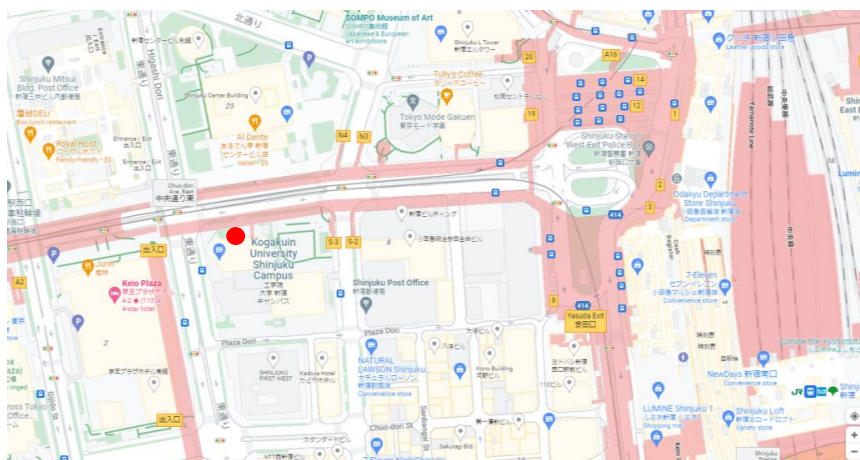


Fig.2 Location of the sampling (red solid circle)

The collected samples were analyzed by using the FIB-TOF-SIMS apparatus, and the shapes of the particles were observed from the images obtained by FIB-TOF-SIMS analysis. Aerosol source data and particle shape characteristics were used to identify the single particle source.

III. Results and Discussion

The results of the FIB-TOF-SIMS analysis of Fe-containing particles-a) and -b). The particle-a) contained Cr and Fe, and a small amount of Cu. It is said that particles from muffler of automobiles contain Mn, Cr, and Fe originated from engine wear and/or engine oil [5]. As for Cu and Ca, they are the markers for brake dust [6]. From these information, the particle-a) was assumed to be automobile origin.

As for the particle-b), the particle contained Li, Na, Al, K and Fe. And SiO₂ and PO₂ were detected as negative ions. The particle containing these components are considered to be of coal combustion origin [7]. However, particles of combustion origin generally exist in a spherical shape. Therefore, the particle-b) is considered to be soil origin because the chemical composition of soil-origin particles containing iron is similar to that of coal combustion-origin particles.

Table 2 shows the source profiles of aerosols surveyed by the Ministry of the Environment in 2015[8]. The existence ratios of the elements constituting the single particle-a) and -b) were compared with those calculated from the source profile. Source data are expressed by weight ratio, and existing ratio was calculated by the ion counts of the TOF-

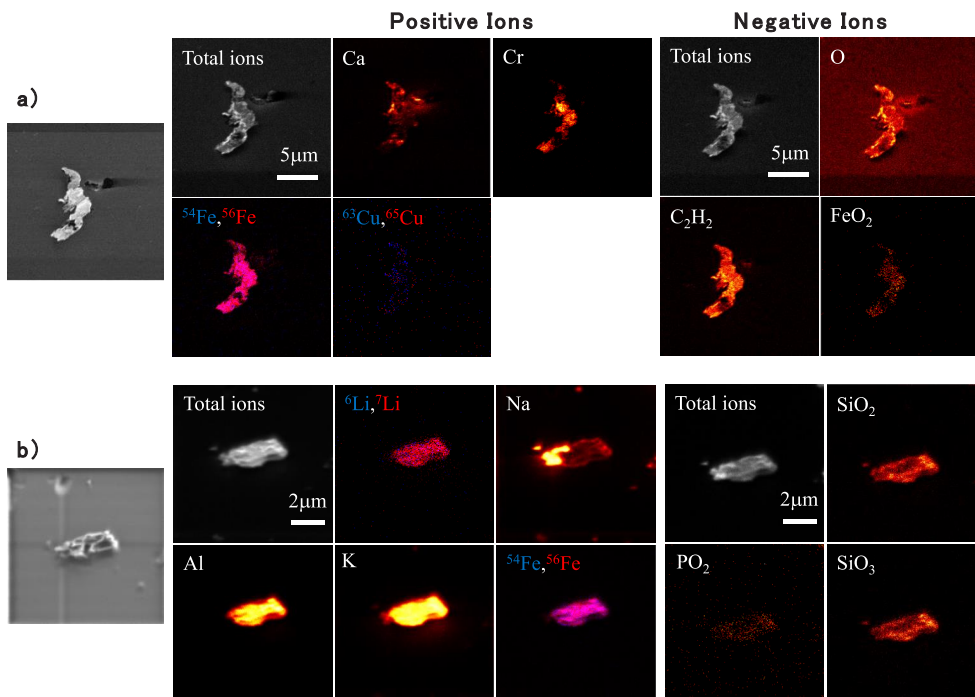


Figure 2: TOF-SIMS images of each elements of collected iron-containing particles.

Table2: Source Data^[8]

Elements	Source data			
	Brake dust		Soil and road dust	
	Concentration (g/g)	existence ratio (%)	Concentration (g/g)	existence ratio (%)
Na	7.6E-03	4.8	1.3E-02	6.6
Al	1.9E-02	12	6.1E-02	31
K	3.5E-03	2.2	1.3E-02	6.6
Ca	3.2E-02	20	5.5E-02	28
V	5.9E-05	0.037	1.1E-04	0.056
Cr	4.2E-04	0.26	2.8E-04	0.14
Mn	7.2E-04	0.45	1.1E-03	0.56
Fe	9.1E-02	57	5.3E-02	27
Zn	3.3E-03	2.1	1.3E-03	0.66
Sb	2.1E-03	1.3	1.3E-05	0.0066

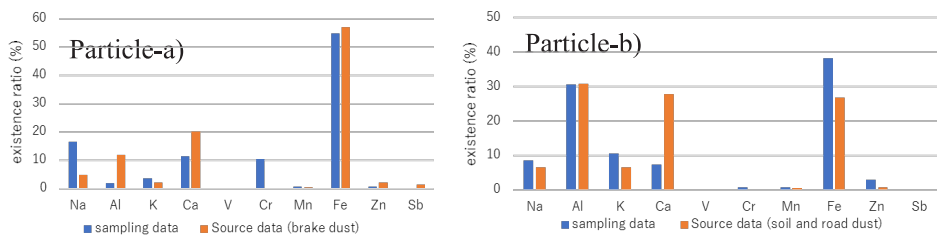


Figure 3: Comparison of elemental abundance ratios between sampled particles and source profiles.

SIMS analysis. In essence, they cannot be compared exactly. However the similarity or correlation can be estimated by this expression.

Figure 3 compares the chemical composition estimated by TOF-SIMS of the particle-a) with the source data of brake dust. Calcium and Fe are the similarity. However, Sb, which is the most characteristic element in brake dust was too small in the TOF-SIMS result. Therefore we cannot confirm it to be brake dust. As for the particle-b), as shown in Fig.3b, it has a certain similarity with the source data of soil and road dust.

In this study, it was confirmed that most of the collected Fe-containing particles were in a state of mixing with salts. Figure 4 shows the FE-SEM image and FIB-TOF-SIMS analysis results of the Fe-containing particles in the same area. It is thought that the primary particles of metallic Fe-containing particles emitted, and were rapidly oxidized in atmosphere, and a liquid coating was formed by the condensed water on the cooled particle surface which resulted in the salts^[9].

IV. Conclusions

The Fe-containing particles collected in Shinjuku were analyzed for their composition and evaluated for their shape characteristics. The observed Fe-containing particles were confirmed to be of automobile origin and soil origin, respectively. In addition, it was

confirmed that salts were attached around the Fe-containing particles. As a future prospect, we would like to perform internal structure analysis by taking advantage of the surface sensitivity of FIB-TOF-SIMS. We also plan to quantitatively show the source of the iron-containing particles.

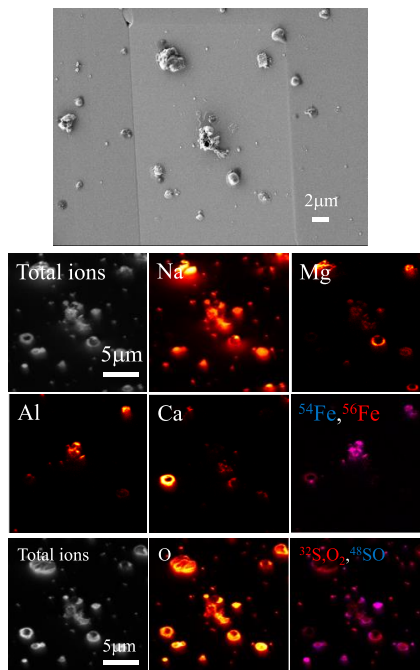


Figure 4: Examples of iron particles with salts around them (right: FE-SEM image, middle: positive, left: negative). The FE-SEM image shows the traces of FIB scraping.

References

- [1] N. Takegawa, A. Takami, *Earozoru Kenkyu*, **32**, 118-124 (2017).
- [2] T. Sakamoto *et al.*, *Appl. Surf. Sci.*, **255**, 1617-1620 (2008).
- [3] E. Vidrio, H. Jung, C. Anasatasio, *Atmos. Environ.*, **42**, 4369-4379 (2008).
- [4] C. Arden Pope *et al.*, *JAMA*, **287**, 1132-1141 (2002).
- [5] Brian J Majestic *et al.*, *Sci total environment*, **407**(18), 5104-5109 (2009).
- [6] Beddows *et al.*, *Atmos. Environ.*, **129**, 167-175 (2016).
- [7] H. Furutani *et al.*, *J. Geophys.*, **116**, D18204 (2011).
- [8] Ministry of the Environment: Fine particulate matter (PM2.5) measurement data|2015 http://www.env.go.jp/air/osen/pm/monitoring/data/pm25_27.html (accessed on December 6, 2021)
- [9] T. Moreno *et al.*, *Environmental Science: Processes & Impacts*, **19**, 59-64 (2017).

Influence of residual Ga₂O₃ and Cs on the increase in the maximum quantum efficiency of NEA-GaAs by a two-step thermal cleaning process

Y. Sada[#], M. Jono, D. Kobayashi, Y. Yoshitake and T. Meguro
*Graduate School of Science, Tokyo University of Science,
1-3, Kagurazaka, Shinjuku-ku, Tokyo 162-8601, Japan*

Abstract

We investigated the relationship between the increase in the maximum quantum efficiency of negative electron affinity (NEA)-GaAs depending on the thermal cleaning conditions and residual species, e.g., Ga₂O₃ and Cs atoms, on the GaAs surface using temperature-programmed desorption. We found that the increase in the maximum quantum efficiency occurs during thermal cleaning at 500–600°C for ~8.5 min. The increase in ratio was maximum when the amount of Ga₂O₃ on the GaAs surface was maximum. In the case that Cs atoms remained, when the thermal cleaning was performed in a temperature range where Ga₂O₃ was not formed, the effect facilitating an NEA surface formation was observed. However, the residual Cs atoms might not be affected at an increased maximum quantum efficiency. From the above results, we considered that the double-dipole structures of Cs-Ga₂O₃ and Cs-O are significant to the high quantum efficiency. The Cs-O dipoles are considered to form easily when Ga₂O₃ is on the GaAs surface before the NEA activation, and the amount of Cs-O dipoles required to reduce the vacuum level below the conduction band minimum increase more than usually NEA surface. As a result, the maximum quantum efficiency increases.

I. Introduction

A negative electron affinity (NEA) surface in which the vacuum level lies below the conduction band minimum is a candidate for the next-generation electron source because of its properties, such as large photoelectron current, ultra-short-pulsed operation, high spin polarization, and low emittance nature. Although various models have been proposed for the NEA surface over more than half a century, the detailed mechanisms of the actual NEA surface are not yet understood.

Generally, an NEA surface is formed by the adsorption of Cs and O atoms on a clean p-type GaAs surface in an ultra-high vacuum condition. After the formation of the NEA surface, the photoelectron current decreases over time because of the adsorption of

[#]e-mail : 1220704@ed.tus.ac.jp

an unexpected residual gas, back bombardment of ionized residual gas, and thermal desorption of the (Cs, O) layer. This sample is repeatedly activated by eliminating the residual species on the surface with thermal cleaning at high temperatures. However, it has been reported that the maximum quantum efficiency of NEA-GaAs increased after thermal cleaning at low temperatures [2nd thermal cleaning (2nd TC)]^{1,2}. Based on this result, we presumed that new photoemission sites are formed on the NEA surface by the residual species on the surface. In particular, Ga₂O₃ plays an important role in increasing the quantum efficiency; however, the effect of other residues (Cs, As, etc.) on increasing the quantum efficiency have not been discussed.

In this study, 2nd TC was performed at several temperatures to investigate the rate of increase in the maximum quantum efficiency of NEA-GaAs, and the effect of the remaining Ga₂O₃ and Cs on the surface on the above experimental results were evaluated using temperature-programmed desorption (TPD). It was found that the rate of the increase in the maximum quantum efficiency correlates with the amount of residual Ga₂O₃. Moreover, when the 2nd TC was performed at a temperature at which Ga₂O₃ was not formed, residual Cs facilitated the NEA surface formation but did not affect the increase in the maximum quantum efficiency.

II. Experimental Procedures

The samples used were epi-ready Zn-doped p-type GaAs (100) ($\sim 1.0 \times 10^{19} / \text{cm}^3$) substrates. The thermal pretreatment of the samples and the successive NEA activation with alternating supply of Cs and O₂ were performed in a UHV chamber. The base pressure of the chamber was kept at $2.0\text{--}4.0 \times 10^{-8}$ Pa. The sample was soldered on a Mo sample holder by pasting an In seat for thermal conduction. The temperature for the thermal pretreatments was elevated using a carbon heater. The temperatures were measured using a chromel–alumel thermocouple in contact with the backside of the sample holder. The Cs atoms were supplied by sublimation from a Cs dispenser (SAES Getters), and the pressure of O₂ (>99.999995 vol.%) was controlled with a variable leak valve. To measure the emitted photoelectron current, the sample was biased by -100 V. The light source was a Hg–Xe lamp, and a monochromatic light ($h\nu = 1.50$ eV, density = $296 \mu\text{W}/\text{cm}^2$) was illuminated using an optical spectrometer. The quantum efficiency was calculated as a simple ratio of the number of emitted photoelectrons to the number of incident photons.

The thermal cleaning was performed at 700°C for ~ 60 min (1st TC). After the sample was cooled down to room temperature, the NEA activation was performed by the “yo-yo” method (1st NEA activation)³. The photocurrent during the NEA activation exhibited cyclic ups and downs corresponding to the supply of Cs and O₂. The peak value

of the photocurrent gradually increased and finally saturated⁴). As the activation process ended, the thermal cleaning was performed at 150°C, 300°C, 430°C, 460°C, 500°C, 525°C, 575°C, 660°C, and 700°C for ~8.5 min (2nd TC). The NEA activation was performed again when the temperature was naturally cooled to room temperature (2nd NEA activation). When the activation process was completed, the sample surface was cleaned by the 1st TC again. In the 1st and 2nd TC processes, the desorbed substances were also analyzed using TPD at a programmed rate of 10°C/min.

III. Results and Discussions

Figure 1 shows the TPD spectra of Cs, As₂, Ga₂O from the 1st NEA-GaAs surface during the 1st TC, and we determined the temperatures of Ga₂O₃ formation and desorption. The horizontal axis represents the temperature of the GaAs sample. The left vertical axis shows the intensity of Cs desorption, and the right vertical axis shows the intensities of As₂ and Ga₂O desorption. In the case of 1st TC, the thermal cleaning was performed at 700°C for ~1 h. The solid, dashed, and dotted lines represent Cs, As₂, and Ga₂O, respectively. The Cs desorption at 600–660°C was not observed because the Cs desorption from other samples except the GaAs sample was removed.

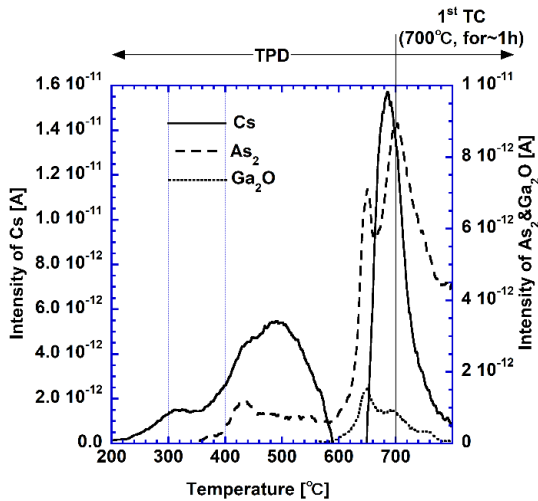
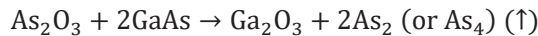


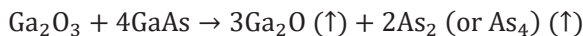
Fig. 1 TPD spectra of Cs (solid line), As₂ (dashed line), and Ga₂O (dotted line) from the 1st NEA GaAs surface during the 1st TC (700°C, for ~1 h).

The Cs desorption began at 200°C, and the As₂ desorption was observed at 350°C. The desorption peaks of Cs and As₂ from 350°C to 600°C were derived from the Cs-O-As compounds^{5,6}. First, an As oxide, As₂O₃, was formed simultaneously with the desorption of Cs. However, As₂O₃ is unstable at a temperature higher than 250°C; therefore, Ga₂O₃ was formed with As₂ desorption according to the following process:



The As₂ and Ga₂O signals were observed in the same temperature range (600–660°C).

This indicates that the following reaction occurred:



Consequently, we considered that Ga_2O_3 was formed at 350°C and desorbed at 600°C in this experiment.

Next, to investigate the relationship between the increase in the maximum quantum efficiency and the amount of residual Ga_2O_3 on the GaAs surface, we discuss the relationship between the increased rates of the maximum quantum efficiency and the amount of As_2 desorbed simultaneously with the formation of Ga_2O_3 . Figure 2 shows the 2nd TC temperature dependence of the rate of increase of the maximum quantum efficiency and the amount of As_2 desorbed at $350\text{--}600^\circ\text{C}$. The horizontal axis represents the temperature of the 2nd TC. The left vertical axis shows the increased rates of the maximum quantum efficiency. When this rate was more than 1, the maximum quantum efficiency of NEA-GaAs increased due to the 2nd TC. The right vertical axis shows the amount of As_2 desorbed after the 2nd NEA activation normalized by the As_2 desorption after the 1st NEA activation at $350\text{--}600^\circ\text{C}$. The smaller the As_2 desorption, the larger the amount of Ga_2O_3 formed on the GaAs surface by the 2nd TC. As shown in Fig. 2, the increase in the maximum quantum efficiency was closely related to the amount of Ga_2O_3 on the GaAs surface. The increased rate of quantum efficiency indicated the maximum value when the amount of As_2 desorbed was minimum, that is, the maximum amount of Ga_2O_3 remained on the GaAs surface and decreased at 660°C and 700°C when Ga_2O_3 was desorbed. Based on the above results, it was concluded that the rate of the increase in the maximum quantum efficiency correlates with the amount of residual Ga_2O_3 .

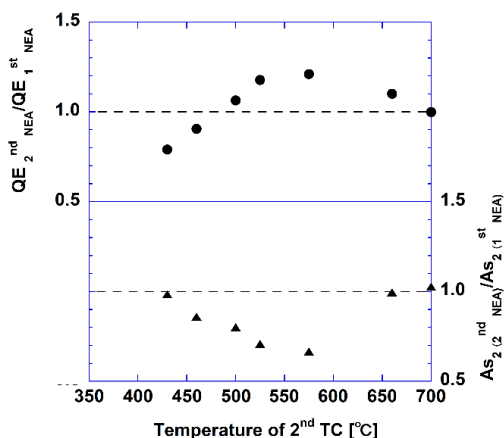


Fig. 2 The 2nd TC temperature dependence of the increasing rates of the maximum quantum efficiency (left vertical axis) and the amount of As_2 desorbed at $350\text{--}600^\circ\text{C}$ normalized by As_2 desorbed after the 1st NEA activation at $350\text{--}600^\circ\text{C}$ (right vertical axis).

Finally, to investigate the effect of residual Cs species on the GaAs surface, we discuss the quantum efficiency during the NEA activation when the 2nd TC was performed

at temperatures at which Cs remained sufficiently. Figure 3 shows the peak quantum efficiency values during the NEA activation when the 2nd TC was performed at 150°C and 300°C for 8.5 min. The horizontal axis represents the number of peaks. Only the first peak was obtained by the Cs supply; the others were obtained by the O₂ supply. The vertical axis shows the peaks of quantum efficiency. The shape of the plot classifies the thermal cleaning conditions; circular plot for 150°C of the 2nd TC, square plot for 300°C of the 2nd TC, and triangular plot for the 1st TC (700°C for 1 h), respectively. Note that in the case of the 2nd TC, the first peaks of quantum efficiency due to the Cs supply were higher than those observed at the 1st TC. According to previous works ³⁾, the NEA surface on GaAs was not formed at the first peak of quantum efficiency and was formed at the other peaks formed by the O₂ supply in the 1st NEA activation. As can be observed in the first peaks at 150°C and 300°C of the 2nd TC in Fig. 3, both the values were higher than the second peak of 1st NEA activation. Therefore, the NEA surface on GaAs was formed by due to only the Cs supply at the 2nd TC at 150°C and 300°C. As the reason for this, it was considered that the Cs species which influence photoelectron emissions, such as Cs-O-Ga and Cs-O-As, etc., sufficiently remained on the GaAs surface. Wu *et al.* reported that Cs-O-Ga and Cs-O-As were desorbed at more than 350°C ⁶⁾. Therefore, it is presumed that the Cs species facilitated the formation of the NEA surface on GaAs. However, no increase in the maximum quantum efficiency was observed. At present, we consider that the residual Cs on the NEA surface does not contribute to the increasing maximum quantum efficiency of NEA-GaAs.

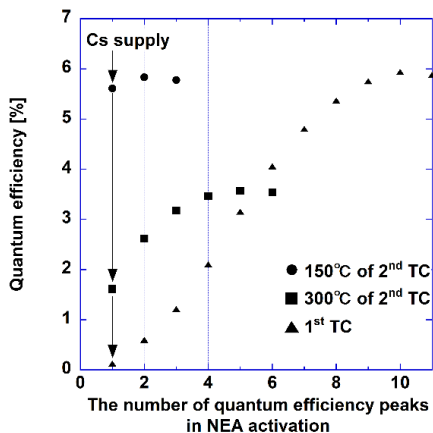


Fig. 3 Peak values of quantum efficiency during the NEA activation when the 2nd TC was performed at 150°C (circular plot) and 300°C (square plot) for 8.5 min, and the 1st TC (triangle plot) was also performed.

The above results indicate that the increase in the maximum quantum efficiency resulted in the residual Ga₂O₃ on the GaAs surface. The double-dipole model, Cs-GaAs or Cs-O-GaAs dipole and (Cs, O) dipole, has been well known as a model of the NEA surface ⁷⁻⁹⁾. In the two dipoles mentioned above, the (Cs, O) dipole is suggested to reduce

the vacuum level below the conduction band minimum. In the case of Ga₂O₃ existing on the surface before the NEA activation, Cs-Ga₂O₃ is formed when Cs is first supplied during the activation process. During the following O₂ exposure, the O atoms dissociated from O₂ react with the Cs atoms and/or GaAs surface. However, it is predicted that the formation of the Cs-O dipole is facilitated rather than the reaction of O atoms and GaAs surface by residual Ga₂O₃. Therefore, the number of Cs-O dipoles increases compared to that in the 1st NEA activation, leading to an increase in the maximum quantum efficiency.

IV. Conclusion

We investigated the relationship between the increase in the maximum quantum efficiency of NEA-GaAs depending on the thermal cleaning conditions and residual Ga₂O₃ and Cs on the GaAs surface. It was found that the increase in the maximum quantum efficiency necessitated Ga₂O₃, and the increasing rate was maximum when the amount of Ga₂O₃ on the GaAs surface was maximum. In the case of residual Cs, when the 2nd TC was performed at a temperature at which Ga₂O₃ was not formed, the residual Cs facilitated NEA surface formation; however, it might not affect the increase in the maximum quantum efficiency. At present, we consider that the Cs-O dipole reduces the vacuum level below the conduction band minimum and is formed easily when Ga₂O₃ is present on the GaAs surface before the NEA activation, which leads to an increase in the maximum quantum efficiency.

ACKNOWLEDGMENT

This work was partially supported by JSPS KAKENHI Grant Number JP 19H00666.

References

- 1) B. J. Stocker, Surf. Sci., **47**, 501, 1975
- 2) Y. Inagaki, and T. Meguro, Jpn. J. Appl. Phys, **59**, 045504, 2020
- 3) S. more, S. Tanaka, Y. Fuji and M. Kamada, Surf. Sci, **527**, 41, 2003
- 4) Y. Sada and T. Meguro, Appl. Surf. Sci, **513**, 145699, 2020
- 5) J. Sakai, G. Mizutani, and S. Ushioda, Appl. Surf. Sci, **64**, 275, 1993
- 6) J. X. Wu, F. Q. Li, J. S. Zhu, Z. M. Wang, M. R. Ji and M. S. Ma, J. Phys.: Condens. Matter, **13**, 8725, 2001
- 7) D. G. Fisher, R. E. Enstrom, J. S. Escher and B. F. Williams, J. Appl. Phys, **43**, 3815, 1972
- 8) C. Y. Su, W. E. Spicer and I. Lindau, J. Appl. Phys, **54**, 1413, 1983
- 9) J. Zou, B. Chang, Z. Yang, Y. Zhang and J. Qiao, J. Appl. Phys, **105**, 013714, 2009

ESTIMATION OF EXCITATION DENSITY OF REPORTED TWO-PHOTON PHOTOLUMINESCENCE INTENSITY DISTRIBUTIONS AT A DISLOCATION IN AN n-GaN LAYER ON A M-3D SUBSTRATE

Kazuhiro Mochizuki[#], Hiroshi Ohta, Fumimasa Horikiri¹, Tomoyoshi Mishima
*Research Center of Ion Beam Technology, Hosei University, 3-7-2, Kajino-cho,
Koganei, Tokyo 184-8584, Japan*

¹ *SCIOCS Co. Ltd., 880, Isagozawa-cho, Hitachi, Ibaraki 319-1418, Japan*

We estimated the excitation density of the reported two-photon photoluminescence from an n-GaN layer on an M-3D substrate by fitting the intensity distributions at a dislocation. We found that all the data points of the intensity distributions were reproduced with the effective dislocation radius of 8 nm. Considering the range of the excess hole concentration (Δp) within which almost all data points fell, we estimated Δp to be $10^{16\pm 1} \text{ cm}^{-3}$.

I. Introduction

Development of high-quality GaN substrates has made it possible to easily fabricate vertical p⁺n diodes on free-standing substrates. A record high breakdown voltage of 5 kV has been achieved in combination with a low on-resistance R_{on} of $1.25 \text{ m}\Omega \text{ cm}^2$ at a forward voltage of 5 V.¹⁾ The quality of substrates has also been improved. For example, low-dislocation-density ($N_{\text{dis}} \leq 4 \times 10^5 \text{ cm}^{-2}$) GaN substrates became available via hydride vapor phase epitaxy (HVPE) and a maskless 3D (M-3D) method.²⁾ To suppress propagation of dislocations from the seed crystal, the M-3D method avoids *c*-plane growth; namely, the initial three-dimensional growth is followed by two-dimensional growth in which growth temperature and partial pressures of gallium chloride and ammonia are changed.²⁾

On M-3D substrates, as well as on conventional substrates by the void-assisted separation (VAS) method,³⁾ Ohta et al. fabricated GaN p⁺n diodes and observed a positive correlation between R_{on} and N_{dis} .⁴⁾ They also observed two-photon photoluminescence (2PPL) from an 8- μm -thick n-GaN (donor density N_{D} : $1 \times 10^{16} \text{ cm}^{-3}$) layer on an M-3D substrate and identified dislocations as dark spots.^{4,7)} The ambipolar lifetime τ_a determined by 2PPL, however, depends on the excitation density, which was not clear with respect to their 2PPL measurement. Accordingly, in this paper, we estimate τ_a and the excess hole concentration (Δp) in the 2PPL measurement reported in Ref. 4.

II. Analysis

The diffusion and recombination of electrons and holes generated by the source $Q(\mathbf{r})$ are described by the following three-dimensional equation

$$D_a \Delta n(\mathbf{r}) - n(\mathbf{r}) / \tau_a + Q(\mathbf{r}) = 0, \quad (1)$$

[#] e-mail: kazuhiro.mochizuki.66@hosei.ac.jp

where D_a is the ambipolar diffusivity. τ_a is expressed from charge neutrality as

$$\tau_a = \tau_{po} [1 + \{ \Delta p / (N_D + \Delta p) \}], \quad (2)$$

where τ_{po} is the hole lifetime under low-injection conditions. Based on anode-radius-dependent forward current/voltage characteristics of GaN p⁺n diodes on an M-3D substrate, Mochizuki et al. extracted Shockley–Read–Hall lifetime τ_{SRH} of 11 ns.⁸⁾ τ_{SRH} is expressed as

$$\tau_{SRH} = (\tau_{no} \tau_{po})^{0.5}, \quad (3)$$

where τ_{no} is the electron lifetime under low-injection conditions. Here τ_{po} and τ_{no} are given as

$$\tau_{po} = (N_t v_{thp} \sigma_p)^{-1}, \quad (4)$$

$$\tau_{no} = (N_t v_{thn} \sigma_n)^{-1}, \quad (5)$$

where N_t is the concentration of a non-radiative recombination center, v_{thp} and σ_p are, respectively, the thermal velocity and capture cross section of holes, and v_{thn} and σ_n are, respectively, the thermal velocity and capture cross section of electrons. At 300 K, σ_p , σ_n , v_{thp} , and v_{thn} , were reported, by Chichibu et al.,⁹⁾ Maeda et al.,¹⁰⁾ and Saini et al.,¹¹⁾ to be $7 \times 10^{-14} \text{ cm}^2$, $3 \times 10^{-13} \text{ cm}^2$, $2.38 \times 10^7 \text{ cm s}^{-1}$, and $2.43 \times 10^7 \text{ cm s}^{-1}$, respectively. Putting these values into Eqs. (3)–(5) results in the following relation:

$$\tau_{SRH} = 0.48 \tau_{po}. \quad (6)$$

The influence of surface recombination can be ignored because the excitation energy in 2PPL is smaller than the bandgap of n-GaN.¹²⁾ The flux to the cylindrical surface of a dislocation can thus be simply calculated. When the carrier-recombination velocity at a dislocation with the effective radius R is S , the normalized photoluminescence intensity at a distance r from a dislocation, $I(r)$, is expressed as¹³⁾

$$I(r) = 1 - K_0(r/(D_a \tau_a)^{0.5}) / [K_0(R/(D_a \tau_a)^{0.5} + (D_a/RS)], \quad (7)$$

$$D_a = [N_D + \Delta p + (n_i^2/N_D) + \Delta p] D_e D_h / \{ D_e (N_D + \Delta p) + D_h [(n_i^2/N_D) + \Delta p] \}, \quad (8)$$

where K_0 is the zeroth order modified Bessel function of second kind, n_i is the intrinsic carrier concentration, D_e is the electron diffusivity, and D_h is the hole diffusivity. D_h was reported to be anisotropic; namely, a ratio of 1.17 for diffusivity perpendicular and parallel to the c -axis.¹⁴⁾ Hall measurement of a c -plane GaN layer is thus suited for determining diffusivity perpendicular to the c -axis. We carried out Hall measurement of a $1 \times 10^{18} \text{ cm}^{-3}$ doped p-GaN layer on an M-3D (0001) substrate and found that the majority hole mobility μ_h was $29 \text{ cm}^2 \text{ V}^{-1} \text{ s}^{-1}$. Since μ_h is typically constant at $[\text{Mg}] < 1 \times 10^{18} \text{ cm}^{-3}$ ¹⁵⁾ and the minority hole mobility was reported to agree with μ_h ,¹⁶⁾ D_h was calculated from the Einstein relation to be $0.75 \text{ cm}^2 \text{ s}^{-1}$ at 300 K. With respect to S , a constant value was assumed by Conolato in their dislocation model of semiconductors.¹⁷⁾ Although this is the case under low excitation conditions, modeling S is complex under high excitation conditions. Here we simply assume S to be as large as the thermal velocities of carriers.¹¹⁾

τ_a and D_a saturate when Δp is less than 10^{13} cm^{-3} or larger than 10^{19} cm^{-3} . As shown in Figs. 1(a) and 1(c), some data points are not within $\Delta p = 10^{16\pm 3} \text{ cm}^{-3}$ under the assumption of $R = 6$ or 10 nm . In contrast, all data points fall within $\Delta p = 10^{16\pm 3} \text{ cm}^{-3}$ when we assume R of 8 nm [Fig. 1(b)]. Considering the Δp range within which almost all data points fall, we estimated Δp being $10^{16\pm 1} \text{ cm}^{-3}$.

III. Conclusions

By fitting the intensity distributions at a dislocation in an n-GaN layer on an M-3D substrate, we estimated the excess hole concentration during the reported two-photon photoluminescence measurement to be $10^{16\pm 1} \text{ cm}^{-3}$.

Acknowledgement

This work was supported in part by the ‘‘Project of GaN technology innovation for enabling decarbonized society and lifestyle’’ funded by the Ministry of the Environment Government of Japan.

References

- 1) H. Ohta, K. Hayashi, F. Horikiri, M. Yoshino, T. Nakamura, and T. Mishima, Jpn. J. Appl. Phys. **57**, 04FG09 (2018).
- 2) T. Yoshida and M. Shibata, Jpn. J. Appl. Phys. **59**, 071007 (2020).
- 3) Y. Oshima, T. Eri, M. Shibata, H. Sunakawa, K. Kobayashi, T. Ichihashi, and A. Usui, Jpn. J. Appl. Phys. **42**, L1 (2003).
- 4) H. Ohta, N. Asai, F. Horikiri, Y. Narita, T. Yoshida, and T. Mishima, Jpn. J. Appl. Phys. **59**, 106503 (2020).
- 5) N. Gmeinwieser, P. Gottfriedsen, U. T. Schwarz, and W. Wegscheider, R. Clos, A. Krtschil, and A. Krost, A. Weimar, G. Bruderl, A. Lell, and V. Harle, J. Appl. Phys. **98**, 116102 (2005).

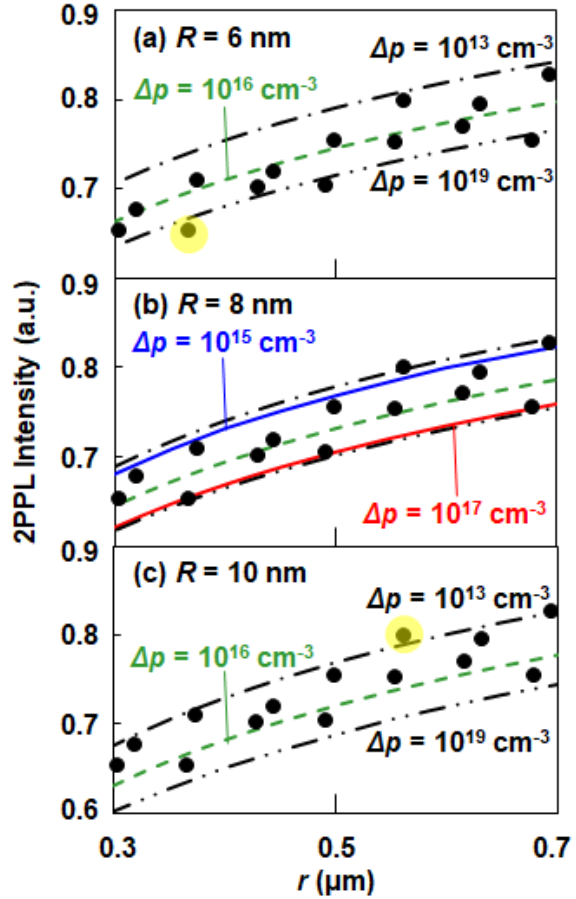


Fig. 1. Measured (symbols)⁴⁾ and fitted (lines) distributions of 2PPL intensity at a dislocation in an n-GaN layer on an M-3D substrate.

R : effective dislocation radius;

Δp : excess hole concentration.

- 6) J. Wang, H. You, H. Guo, J. Xue, G. Yang, D. Chen, B. Liu, H. Lu, R. Zhang, and Y. Zheng, *Appl. Phys. Lett.* **116**, 062104 (2020).
- 7) D.-S. Jiang, D.-G. Zhao, and H. Yang, *Phys. Stat. Solidi (b)* **244**, 2878 (2007).
- 8) K. Mochizuki, H. Ohta, F. Horikiri, and T. Mishima, <https://doi.org/10.1002/pssb.2021002>
- 9) S. F. Chichibu, A. Uedono, K. Kojima, H. Ikeda, K. Fujito, S. Takashima, M. Edo, K. Ueno, and S. Ishibashi, *J. Appl. Phys.* **123**, 161413 (2018).
- 10) T. Maeda, T. Narita, H. Ueda, M. Kanechika, T. Uesugi, T. Kachi, T. Kimoto, M. Horita, and J. Suda, *Jpn. J. Appl. Phys.* **58**, SCCB14 (2019).
- 11) D. K. Saini, Degree Thesis, Wright State University, Ohio, USA, July, 2015.
- 12) T. Tanikawa, K. Ohnishi, M. Kanoh, T. Mukai, and T. Matsuoka, *Appl. Phys. Express* **11**, 031004 (2018).
- 13) K. K. Sabelfeld, V. M. Kaganer, C. Pfüller, and O. Brandt, *J. Phys. D: Appl. Phys.* **50**, 405101 (2017).
- 14) P. Ščajev, K. Jarašiūnas, Ü. Özgür, H. Morkoç, J. Leach, and T. Paskova, *Appl. Phys. Lett.* **100**, 022112 (2012).
- 15) M. Horita, S. Takashima, R. Tanaka, H. Matsuyama, K. Ueno, M. Edo, T. Takahashi, M. Shimizu, and J. Suda, *Jpn. J. Appl. Phys.* **56**, 031001 (2017).
- 16) K. Kumakura, T. Makimoto, N. Kobayashi, T. Hashizume, T. Fukui, and H. Hasegawa, *Appl. Phys. Lett.* **86**, 052105 (2005).
- 17) C. Donolato, *J. Appl. Phys.* **84**, 2656 (1998).

AUTHOR INDEX

G	GOMYO N.	6	N	NAKATA J.	1
	GOTO T.	10	O	OHTA H.	27
H	HANADA S.	10	S	SADA Y.	21
	HORIKIRI F.	27		SAITO M.	10
	HOSHINO Y.	1		SAITO R.	10
I	JONO M.	21		SAKAI K.	16
K	KATOH N.	16		SAKAMOTO T.	6,10,16
	KAWASUGI A.	6		SEKI Y.	1
	KOBAYASHI D.	21		SHU M.	10
	KOJIMA N.	10	T	TAKEUCHI H.	10
M	MATSUSHIMA K.	10	Y	YOSHIHARA M.	1
	MEGURO T.	21		YOSHITAKE Y.	21
	MISHIMA T.	27			
	MOCHIZUKI K.	27			
	MORITA M.	6,10,16			

法政大学イオンビーム工学研究所
TEL 042(387)6094

〒184-8584 東京都小金井市梶野町3-7-2
FAX 042(387)6095